Crosshatched nanofibre membranes for direct contact membrane distillation

S. Kim *[a], D. E. Heath [b], S. E. Kentish [a]

[a] Department of Chemical Engineering, The University of Melbourne, Parkville, VIC 3010, Australia

[b] Department of Biomedical Engineering, The University of Melbourne, Parkville, VIC 3010, Australia

Graphical abstract

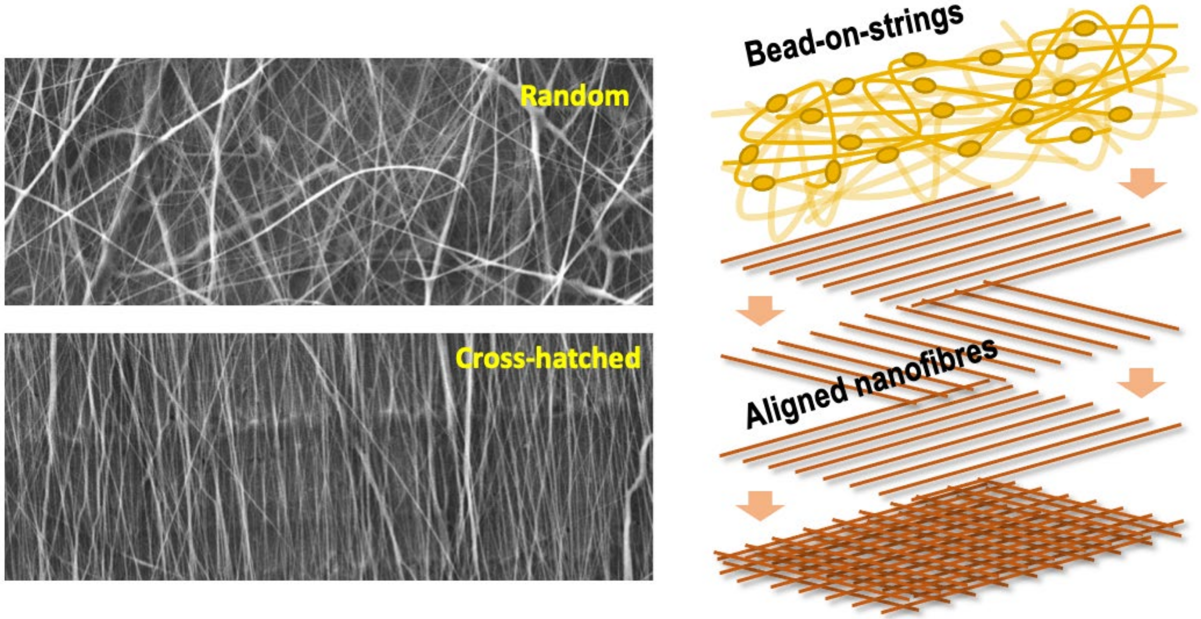

Highlight

- PVDF-HFP crosshatched nanofibres demonstrate enhanced water flux in direct contact membrane distillation.
- The crosshatched structures reduce membrane resistance for water flow while increasing mechanical strength.
- Bead-on-string structures further increase membrane hydrophobicity.
- Stable performance in membrane distillation for up to 100 h at 70 °C.

Abstract

We develop crosshatched nanofibre membranes from hydrophobic polymer, poly(vinylidene fluoride-hexafluoro propylene) (PVDF-HFP) for direct contact membrane distillation. The membranes are fabricated with a unique crosshatched structure that is achieved by lamination of alternating layers of aligned electrospun nanofibres. This membrane structure significantly improves water flux by reducing the tortuosity of the membrane and increases mechanical strength compared to electrospun structures with a random fibre orientation. In addition, we fabricate the top layer of the membrane using electrospun fibres with a bead-on-strings morphology which further increases the hydrophobicity by increasing the surface roughness, minimising pore wetting. Herein, we illustrate that the crosshatched nanofibre membranes with the bead-on-strings structure exhibit great water flux and mechanically robust structures for continuous operations, resulting in a water flux of 65 kg m^{-2} h^{-1} and 99.99 % rejection with steady performance over 100 h.

Keywords:

PVDF, electrospinning, crosshatched nanofibers, membrane distillation, desalination

1. Introduction

Membrane distillation (MD) is a promising approach to desalination. Ideally, it operates at a small scale and uses carbon-free and renewable energy such as solar or industrial waste heat [1-4]. Such MD technology has already been demonstrated at a pilot scale using solar energy, with the system producing 19.6 m^3 of potable water per year from the spiral-wound membrane unit of 7.2 m^2 [5]. A MD system thermally draws water vapour from saltwater at 50-80 °C using microporous and hydrophobic membranes within a vapour pressure driving force. Only water vapour should permeate through the membrane while liquid water is retained. This requires a membrane with adequate hydrophobicity for the process to operate optimally [6]. When liquid water penetrates the pores (i.e., pore wetting) the salts in the feed solution also permeate the membrane, so that the process loses significant salt rejection performance [7-9]. Most membranes in laboratory or pilot plant trials are prepared from hydrophobic polymers [10]. Among them, polyvinylidene difluoride (PVDF) is a particularly attractive material because it can be dissolved in typical organic solvents for solution-based fabrication. However, the membranes for MD should ideally be superhydrophobic to further prevent membrane wetting during long operation [11, 12]. Superhydrophobic surfaces are often produced by treating the membrane with fluoroalkyl substances or by structurally modifying the membrane surface [11].

Electrospinning is a method to produce nanofibres using an electric potential derived from a sufficiently high voltage difference [13-15]. Electrospun nanofibres have several advantages for MD including large surface area porosity in comparison with conventional asymmetric membranes. Moreover, control of the structure of the nanofibres during fabrication can be used to modify membrane properties such as tortuosity or hydrophobicity. For example, the crosshatching of the highly aligned nanofibres reduces the intrinsic tortuosity of electrospun nanofibres [16, 17]. The dispersion of nano- or micro-sized particles on polyimide nanofibres by electrospraying improved the hydrophobicity by increasing surface roughness [18]. The additional bead-on-string layer on a nanofibre mat also increased the hydrophobicity, preventing membrane wetting for membrane gas absorption applications [19]. A similar approach to the bead-on-string membranes was investigated in MD using a polystyrene/poly(dimethylsiloxane) blend and PVDF nanofibres, and these membranes improved water flux and long-term performance because of their increased contact angle [20, 21]. However, the membrane ultimate tensile strength was reduced from 7.7 to 1.4 MPa as the diameter of nanofibres decreased [20]. Although the mechanical strength of membranes is less significant for MD applications, a robust nanofibre structures is essential for adequate membrane lifetime.

We have previously reported that crosshatched nanofibre structures can result in improved mechanical properties, as evidenced in a reverse osmosis application [17]. The lamination of aligned polysulfone nanofibres increased the tensile strength three fold, withstanding an applied pressure over 50 bars [17]. This approach may be practical for MD, ensuring mechanical strength. Although MD does not require the same capacity to tolerate high pressure differentials as reverse osmosis, adequate mechanical properties are essential to withstand the stress applied during module preparation [22].

In this study, we report poly(vinylidene fluoride-hexafluoro propylene) (PVDF-HFP) nanofibres with novel crosshatched structures for direct contact membrane distillation (DCMD). As a copolymer of PVDF, the amorphous HFP domain in PVDF-HFP provides superior hydrophobicity due to its high fluorine content, higher solubility and lower crystallinity, which makes it attractive as a membrane material for MD [19]. The crosshatched and random nanofibres are prepared by modifying electrospinning parameters, which influence the tortuosity of nanofibres to improve water flux. A surface layer of PVDF-HFP nanofibres with bead-on-string morphology is deposited on top of the neat nanofibres to further prevent pore wetting by increasing hydrophobicity.

2. Materials and methods

2.1. Materials

The following polymer and reagents were obtained from Merck Pty Ltd (Darmstadt, Germany) and used without purification: PVDF-HFP, N,N-dimethylacetamide (DMAc, 99.8%), acetone (99.5%) and isopropyl alcohol (IPA, 99.5%). Ethanol (99.5%) and sodium chloride (NaCl) were obtained by Thermo Fisher Scientific Australia Pty Ltd (Scoresby, Australia). High purity nitrogen (N_2, 99.999%) gas was purchased from Core Gas (Thomastown, Australia). Deionised water was supplied using a Milli-Q® Direct Water Purifier (Millipore, Burlington, MA).

2.2. Electrospinning of PVDF-HFP nanofibres

Polymer solutions were prepared by dissolving PVDF-HFP pellets (M_w 455,000) in the DMAc and acetone (7:3 w/w) at a concentration of 22 wt% for the neat nanofibres and 12 wt% for the bead-on-strings nanofibres [19]. A custom built electrospinning device was used to prepare the electrospun PVDF-HFP membranes. The device consists of a single syringe pump (Adelab Scientific, Thebarton, Australia), a grounded rotating collector (15 cm diameter and 15 cm length) and a high voltage supply (Spellman CZE 1000R, Hauppauge, NY). The syringe injector is located on a Linear Positioning Stage (Thorlabs NRT150, Newton, NJ), horizontally moving at 1.66 mm s^{-1} to uniformly translate nanofibres on the collector. The distance between the needle tip and the collector is set to 10 cm. The applied voltage at the needle was fixed at 12 kV and the polymer solution was injected at 1.0 mL h^{-1}. The collector was rotated at 13.3 m s^{-1} for the aligned nanofibres, as determined in our previous report [17].

The cross hatched electrospun structures were generated by depositing alternating layers of orthogonally aligned nanofibres. Briefly, a layer of aligned nanofibres was deposited using 0.8 mL of polymer solution onto aluminium foil attached on the rotating collector with an area of 225 cm^2. After deposition of the first layer of fibres, the foil was detached, rotated by 90° and re-attached to the collector. The next layer of the aligned nanofibres was produced under the same conditions to create a new layer of aligned fibres that are oriented orthogonally to the first layer. The crosshatched nanofibre (CNF) membrane was obtained by depositing eight alternating layers of nanofibres. Finally, a top layer of nanofibres with a bead-on-string morphology was deposited on top of the CNF membrane by electrospinning 0.5 mL of a 12 wt% solution at 1.6 m s^{-1}. The crosshatched nanofibre membrane with the bead-on-string top layer is referred to as CNF-BS. As a comparison, random nanofibre (RNF) membranes and RNF membranes with bead-on-strings (RNF-BS) were prepared at the same conditions as above while applying a lower rotation speed of 1.6 m s^{-1} and without changing the position of the aluminium coupon.

PVDF-HFP asymmetric membranes were also prepared as a conventional membrane by phase inversion from a 20 wt% solution in DMAc using a glass plate and an ethanol bath as coagulant. The thickness of the asymmetric membrane was adjusted to 80 μm using a film casting knife (Adjustable Film Applicator, BYK Instruments, Geretsried, Germany).

2.3 Characterisation

We employed scanning electron microscopy (SEM) to observe the membrane structures (SEM, FlexSEM, Hitachi, Tokyo, Japan). The hydrophobicity of the membranes was assessed by measuring the contact angle of the membrane surface with a tensiometer (OGA 20, Dataphysics, Charlotte, NC). A universal testing machine was employed for the mechanical strength in accordance with the ASTM D638 standard (Model 5944 2 kN, Instron, Norwood, MA). An HP4750 stirred cell from Sterlitech was used to investigate the water permeability and breakthrough pressure. The feed pressure was levitated in a stepwise manner at 5 kPa intervals to measure the value at which breakthrough occurred. Each pressure was held for 10 minutes to allow equilibration at that pressure.

The Young-Laplace equation was used to determine the maximum pore size (d_{max}) from the breakthrough pressure, assuming sufficiently narrow and circular pores with diameter of d_{max} [23].

$$p_B = \frac{4 \cdot \gamma \cdot cos\theta}{d_{max}} \tag{1}$$

where θ and γ are a liquid contact angle and surface tension, respectively. This equation is only applicable when the contact angle is lower than 90°, so a 20 wt% isopropyl alcohol solution with a surface tension of 34 mN m^{-1} was used for characterisation of the hydrophobic surface.

A gas permeance measurement using nitrogen was employed to investigate the average pore size ($d_{average}$) by Knudsen flow and Poiseuille flow, using an equation defining the gas permeance (j_i, mol m^{-2} Pa^{-1} s^{-1}) as a function of pressure (p), gas constant (R, J mol^{-1} K^{-1}), applied temperature (T, K), gas molecular weight (M), porosity (ε), pore radius (r_p), effective pore length (L_P) and viscosity (μ_i, 0.0000178 Pa s at 25 °C), as below [24].

$$j_i = \frac{2 \cdot r_p \cdot \varepsilon}{3 \cdot R \cdot T \cdot L_p}\left(\frac{8 \cdot R \cdot T}{\pi \cdot M}\right)^{0.5} + \frac{r_p^2 \cdot \varepsilon}{8 \cdot \mu_i \cdot R \cdot T \cdot L_p} \cdot p \tag{2}$$

$$j_i = K_0 + P_0 \cdot p \tag{3}$$

From Equations (2) and (3),

$$r_p = \frac{16}{3} \cdot \left(\frac{P_0}{K_0}\right) \cdot \left(\frac{8 \cdot R \cdot T}{\pi \cdot M}\right)^{0.5} \cdot \mu_i \tag{4}$$

$$d_{average} = 2 \cdot r_p \tag{5}$$

$$\frac{\varepsilon}{L_p} = \frac{8 \cdot \mu_i \cdot R \cdot T \cdot P_0}{r_p^2} \tag{6}$$

ε of the membranes was measured from the sample weight using kerosene [18].

$$\varepsilon = \frac{W_w - W_d}{A \cdot d \cdot \rho} \tag{7}$$

where W_w and W_d (g) are the weight of the wet and dry samples, respectively, A (m^2) is the membrane area, d (μm) is the thickness of the membrane and ρ is the density of kerosene (0.8 g cm^{-3}).

The tortuosity (τ) of the membranes was determined from the water permeability (P_W, L m^{-2} h^{-1} bar^{-1}), measured at 2 bar, by the Hagen-Poiseuille equation [25].

$$P_w = \frac{\varepsilon \cdot r_p^2}{8 \cdot \mu \cdot \tau} \cdot \frac{\Delta p}{d} \tag{8}$$

where Δp is a pressure difference for the measurement of P_w and μ is water viscosity (1.004 mPa s).

The structural parameter (S, μm) is determined as below [26].

$$S = \frac{d \cdot \tau}{\varepsilon} \tag{9}$$

MD can also involve the crystallisation of salt because of the rapid concentration changes within the membrane boundary layer. The concept of heterogeneous nucleation is introduced to explain the formation of crystals. Ideally, well-ordered crystals are formed in an extremely pure solutions by homogeneous nucleation. However, the crystallisation on membrane surface in MD occurs by heterogeneous nucleation due to the interactions between the membrane surface and solutes lowering the activation energy for nucleation. When the interaction is strong due to large contact area, i.e., a water-based solute on hydrophilic membranes with small contact angle, crystals form on the surface by heterogeneous nucleation, eventually resulting in declining water flux. The ratio between the free energy for heterogeneous (ΔG_{het}) and homogeneous (ΔG_{hom}) nucleation on porous membranes can be described with the porosity and contact angle as below [27-29].

$$\frac{\Delta G_{het}^{*}}{\Delta G_{hom}^{*}} = \frac{1}{4} \cdot (2 + cos\theta) \cdot (1 - cos\theta)^2 \cdot \left[1 - \varepsilon \cdot \frac{(1 + cos\theta)^2}{(1 - cos\theta)^2}\right]^3 \qquad (10)$$

2.4 Membrane distillation performance

Desalination performance of the nanofibre membranes was investigated within DCMD by a small scale testing system. As described in **Fig. 1**, a membrane of area 42 cm^2 is positioned in the polytetrafluoroethylene (PTFE) membrane holder (CF042P, Sterlitech, Auburn, WA) with one channel for water flow connected to a feed pump (Hydra-cell G10, Wanner Engineering, Minneapolis, MN) and another for permeate flow (83589 GC-M35.PVS5, Micropump Inc., Vancouver, WA). Simulated seawater with 3.5 wt% NaCl solution and deionised water were used in the feed and permeate tank, respectively. The permeate solution was at 20 °C, whereas the temperature of the feed solution was varied from 50 to 80 °C to generate a vapour pressure difference. The feed flowrate was controlled between 20 to 200 mL min^{-1}. The water flux in this DCMD system was measured by the weight of the permeate tank. NaCl concentration was monitored from its conductivity using a Seven Excellence meter from Mettler Toledo (Columbus, OH) to determine the salt rejection. Since the salt concentration increased due to the water flow from the feed to permeate, additional purified water was supplied to the feed for constant NaCl concentration during measurement.

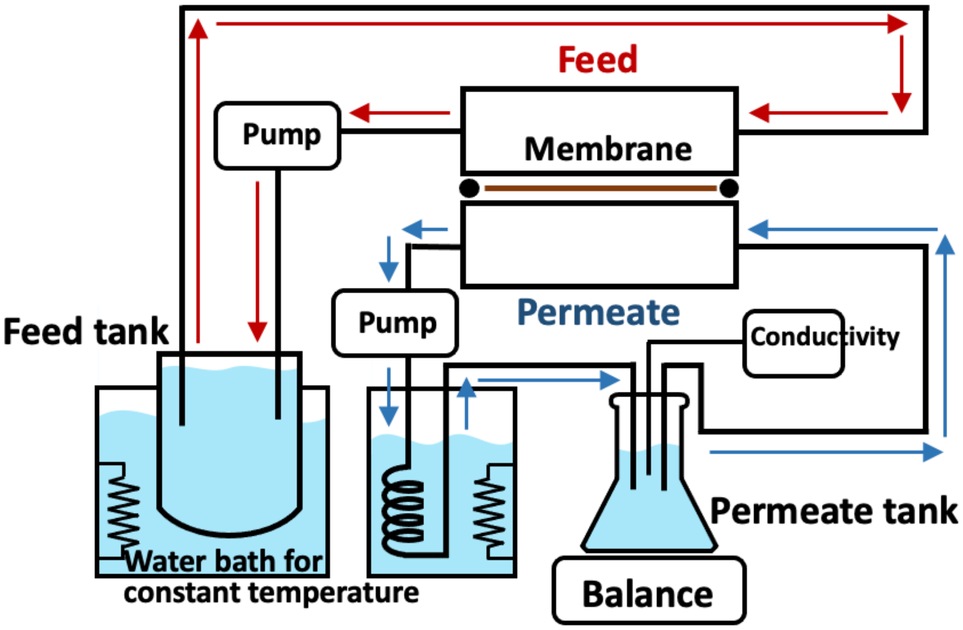

Fig. 1. Illustration of the DCMD testing unit for the flat sheet membranes.

3. Results and discussion

3.1. Characterisation of the nanofibres

The optimum conditions for electrospinning in terms of polymer concentration, applied voltage, or tip-to-collector distance were selected based on our previous publication [19]. **Fig. 2** shows the morphology of the PVDF-HFP nanofibers in random, crosshatched, and bead-on-string format. The nanofibres resulting from 22 wt% solution had diameter around 700 nm, whereas the bead-on-string nanofibers prepared from 12 wt% solution showed a diameter of 300 nm as strings along with bead diameters of 1 to 2 μm. Nanofibres with regular fibre diameter usually provide uniform pore sizes and mechanical strength, preferrable for membrane applications [11]. The beaded fibres result from an unstable polymer solution jet during electrospinning, which weakens the mechanical strength of the resulting membranes. However, these composite structures increase surface hydrophobicity which in turn minimises membrane resistance by preventing wetting [19]. As shown in **Fig. 3** the nanofibrous morphology provides an increased contact angle as compared to the asymmetric membranes and the bead-on-string structures further improves the hydrophobicity. The contact angle is mainly determined by the solid-liquid interfacial energy [29] and the intrinsic surface energy of PVDF-HFP is thus a major determinant. The nanofibre diameter also influences the contact angle, by changing the contact area of liquid droplets on the membrane surface.Nanofibre membranes with similar fibre diameters prepared from this material thus have similar contact angles regardless of the nanofibre orientation.

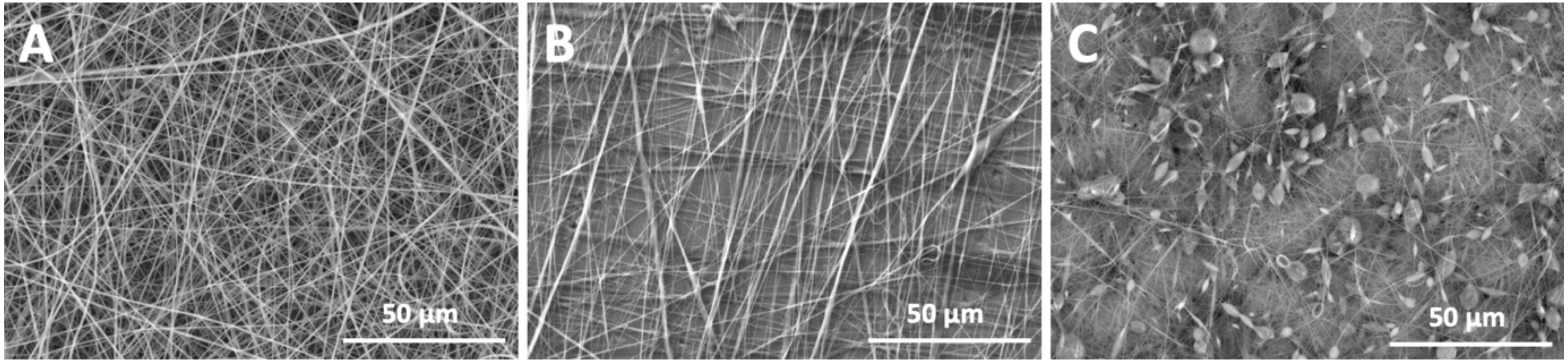

Fig. 2. Morphology of the electrospun membranes in different morphology in (a) random, (b) crosshatched, and (c) bead-on-string nanofibres.

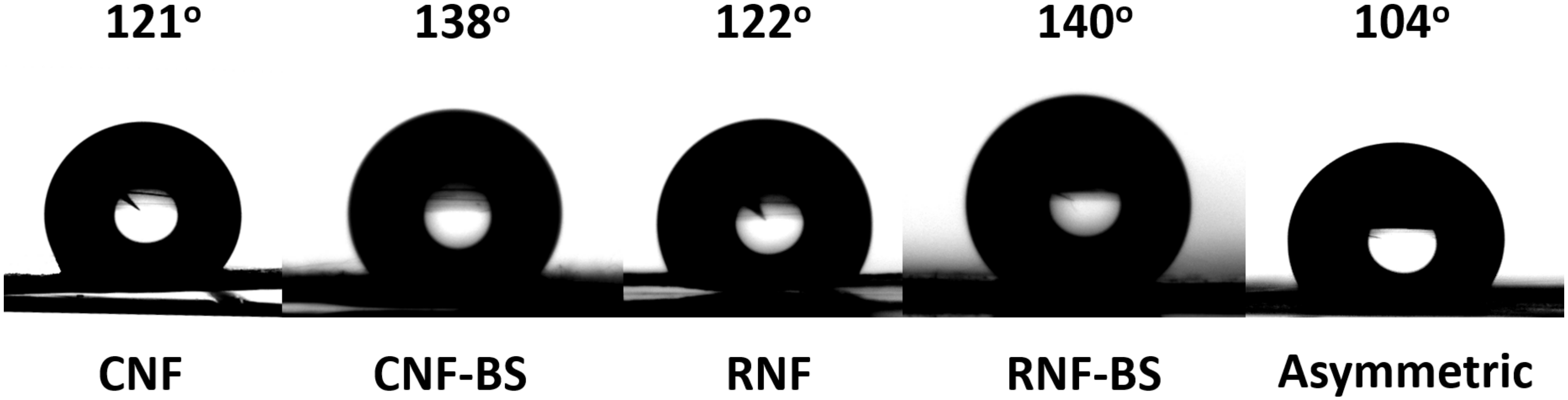

Fig. 3. Water contact angle of PVDF-HFP membranes.

Membrane thickness is a key parameter for the breakthrough pressure and mechanical strength. Thicker membranes provide increased mechanical strength but also reduce water flux by increasing the resistance for molecular transport [18]. The breakthrough pressure, i.e., liquid entry pressure or wetting pressure, is an indication of membrane failure in MD, as it indicates breakthrough of liquid saline water [9]. As the volume of deposited polymer solution increases, the thickness and breakthrough pressure of the resulting membranes also increases as described in **Fig. 4**. The breakthrough pressure of the CNF membranes is related to the reinforcement of the aligned nanofibers with at least 3 or 4 layers required for the reinforced structures to withstand any applied pressure. Similarly, at least 4mL of polymer solution was required for the RNF membranes to be able to withstand an applied pressure. A breakthrough pressure of just under 140 kPa was achieved for both RNF and CNF membranes of around 100 micron in thickness. The membrane breakthrough pressure should, at least, be higher than atmospheric pressure (100 kPa) as the feed and permeate flows generate a slight hydraulic pressure during MD operation [8]. Based on this analysis, the thickness of all PVDF-HFP membranes was controlled to around 80 μm (10 mL of polymer solution for RNF or 8 layers for CNF) for further characterisation.

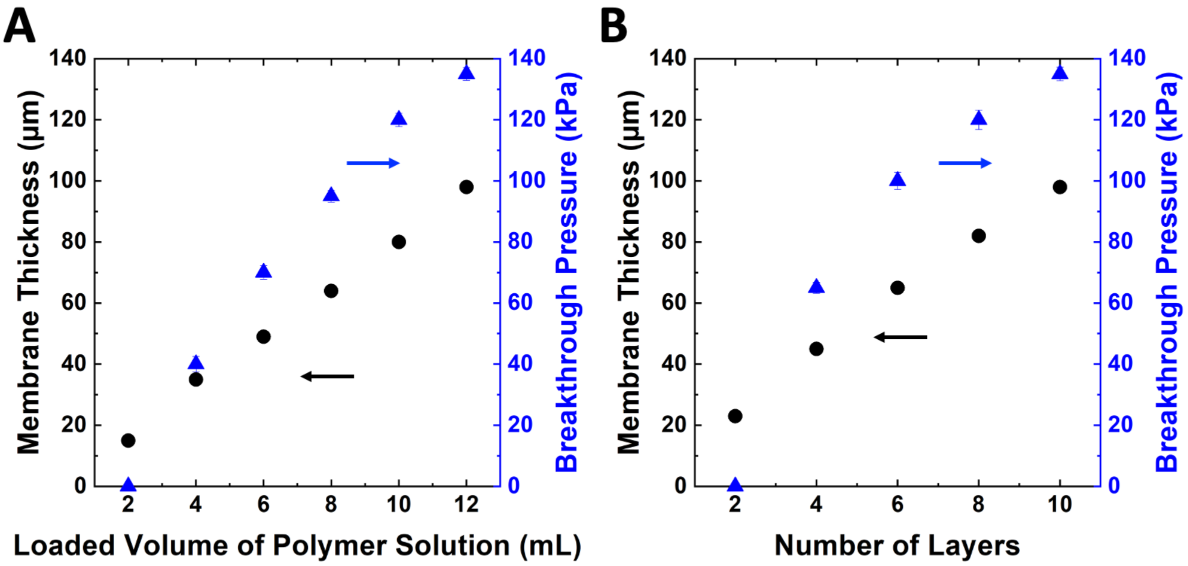

Fig. 4. Thickness and breakthrough pressure of (a) RNF and (b) CNF membranes by loaded solution volume.

For the CNF membranes, three orientations at 0, 45 and 90° were applied to the fibre direction to investigate the fibre alignment on mechanical properties. The elastic properties and toughness of the nanofibres were significantly affected by this nanofibre orientation and also by the testing direction (**Fig. 5** and **Table S1**). The CNF membranes were able to support a load in the direction of fibre alignment (0 or 90°) nearly three times greater than fibres aligned at a 45° angle. However, the elongation was limited due to the large number of nanofibres in the direction of the applied load [30]. Conversely, the CNF membranes aligned at 45° exhibited a 2.5-fold increase in elasticity compared to the 0 or 90° angles. In contrast, the RNF membranes showed isotropic mechanical properties due to the randomly oriented fibres. The improved mechanical properties of the CNF membranes could benefit the membrane in module fabrication and provide resilience with extended lifespan.

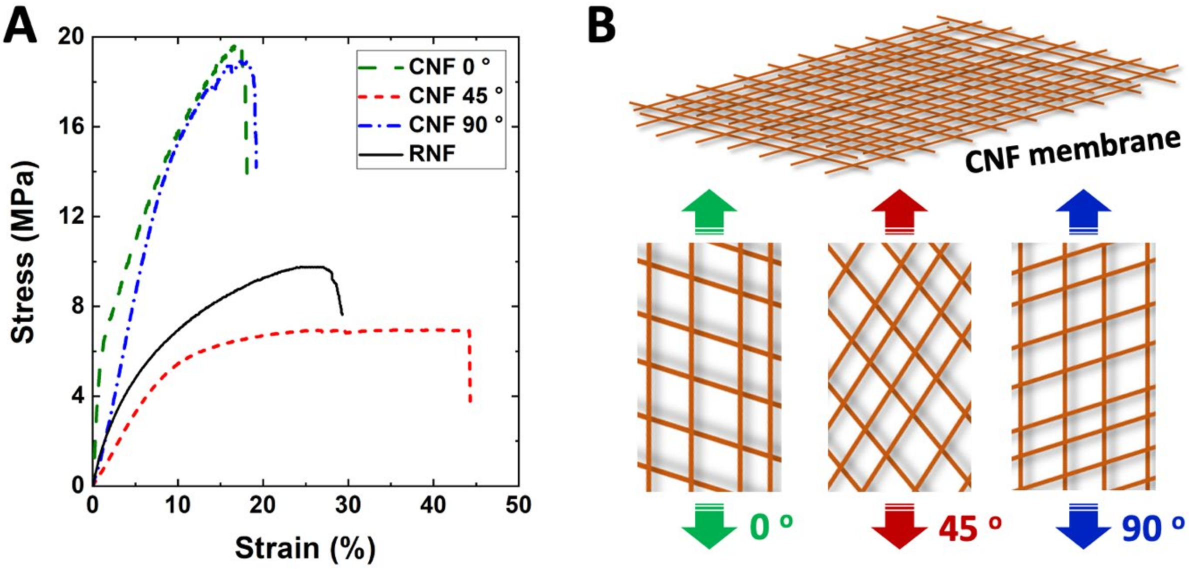

Fig. 5. (a) Representative stress-strain behaviour of the CNF and RNF membranes and (b) their load directions in CNF membranes.

One of the main advantages of nanofibre membranes is their high porosity as compared with asymmetric membranes [19]. In this contribution, both CNF and RNF membranes have very high porosity, around 80 %, as compared to the asymmetric membrane at 62%, despite the similar membrane thickness (**Table 1**). The nanofibre orientation, whether crosshatched or random, does not affect the porosity and contact angle, however, the additional layer of the bead-on-strings further increased the hydrophobicity since the dispersed beads decreased the surface energy due to increased surface roughness. Both the maximum and average pore diameters (d_{max} and $d_{average}$) are larger for the nanofibres than that of the asymmetric membrane. Although the effective surface porosity (ε/L_p) of the asymmetric membrane is larger than that of the nanofibres, it is comparable. Much smaller pore sizes would reduce the water flux in MD [26]. The tortuosity of the nanofibre membranes approaches 1.0, minimising the membrane resistance for mass transfer. Indeed, the crosshatched morphology reduces the tortuosity by 30% from 1.61 to 1.14, which is also significantly lower than that reported for other random nanofibre membranes, such as polyacrylonitrile (1.62) [31], poly(ether sulfone) (1.33) [32], poly(vinyl alcohol) (1.20) [33], PVDF (2.5), or polysulfone (2.0) [34]. The additional bead-on-string layer slightly increased this tortuosity due to its random morphology. The structural parameter, which is related to the porosity, tortuosity, and thickness of membrane, indicates the overall membrane resistance. In MD, this structural parameter directly relates to the membranes resistance and has a strong influence on the water flux.

Table 1. The characteristics of the prepared PVDF-HFP membranes.

	CNF	CNF-BS	RNF	RNF-BS	Asymmetric
Thickness (μm)	82 ± 1	81 ± 1	80 ± 1	82 ± 1	80 ± 1
Porosity, ε (%)	81 ± 2	82 ± 1	82 ± 1	83 ± 2	62 ± 2
Water contact angle (°)	121 ± 2	138 ± 2	122 ± 2	140 ± 2	104 ± 2
Breakthrough pressure of water (kPa)	120 ± 3	140 ± 2	120 ± 2	135 ± 3	350 ± 1
Contact angle of IPA 20 wt% solution (°)	82 ± 1	84 ± 2	82 ± 2	83 ± 3	77 ± 2
Breakthrough pressure of IPA solution (kPa)	38 ± 2	40 ± 2	40 ± 1	42 ± 2	145 ± 2
d_{max} (μm)	0.50	0.36	0.47	0.40	0.21
$d_{average}$ (μm)	0.38	0.34	0.41	0.39	0.17
ε/L_p (m^{-1})	158	150	152	145	210
P_w (L m^{-2} h^{-1} bar^{-1})	14,000 ± 200	10,500 ± 100	12,000 ± 200	9,900 ± 100	410 ± 50
Tortuosity (-)	1.14	1.25	1.61	1.74	6.12

Structural parameter, S (μm)	116	123	157	172	790

The effective area of evaporation can be used to characterise the water flux in MD. This area can be expressed in terms of the effective area per pore, if cylindrical pores of uniform size are assumed and that the gas-solution interface has a spherical shape at the pore entrance (**Fig. 6**) [29] (Eqs. 11-13).

$$Effective\ area\ per\ pore = 2 \cdot \pi \cdot R \cdot h = 2 \cdot \pi \cdot \frac{r_p^2 \cdot (1 - sin\theta)}{(cos\theta)^2} \tag{11}$$

$$Total\ number\ of\ pores\ on\ unit\ area = \frac{A \cdot \varepsilon}{\pi \cdot r_p^2} \tag{12}$$

$$Effective\ area = 2 \cdot \pi \cdot \frac{r_p^2 \cdot (1 - sin\theta)}{(cos\theta)^2} \cdot \frac{A \cdot \varepsilon}{\pi \cdot r_p^2} \cdot \frac{1}{A} = \frac{2 \cdot \varepsilon \cdot (1 - sin\theta)}{(cos\theta)^2} \tag{13}$$

Even though the pores with larger radius have larger effective area per pore, the total porosity and contact angle are the main parameters that determine the effective area (Eq. 13). The effective area of evaporation as a function of contact angle and pore sizes is described in **Fig. 7,** with the data for the current experimental membranes superimposed. Despite the reduced pore diameter with the additional layer of bead-on-strings, the greater hydrophobicity of CNF-BS and RNF-BS increases the effective area, which is preferable for faster evaporation. All the nanofibre membranes exhibit significantly greater effective area than the asymmetric membranes, which can result in higher water flux in DCMD.

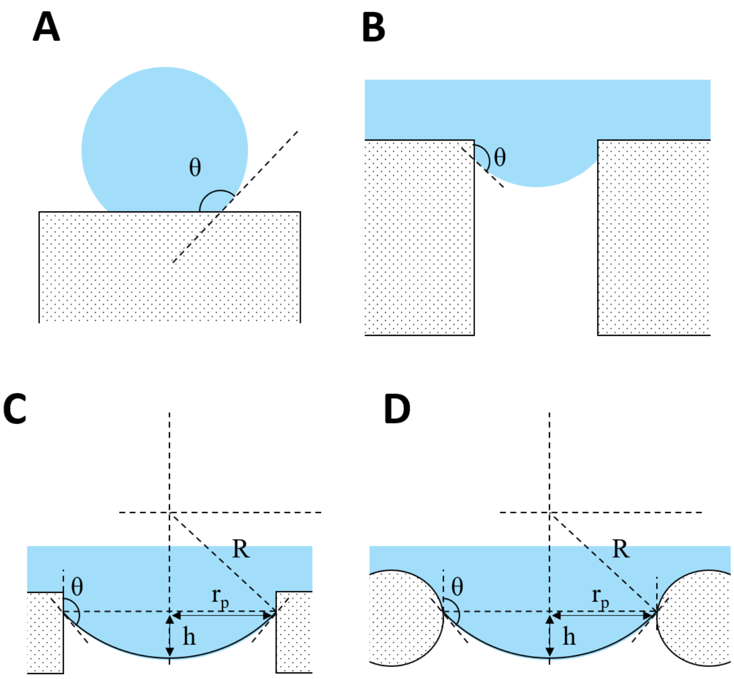

$$R = -\frac{r_p}{cos\theta} \qquad h = -\frac{r_p(1 - sin\theta)}{cos\theta}$$

Fig. 6. Schematic illustration of a solution droplet (a) on non-porous surface, (b) inside a porous membrane for the effective area of evaporation. A pore on (c) asymmetric membranes and (d) nanofibre membranes

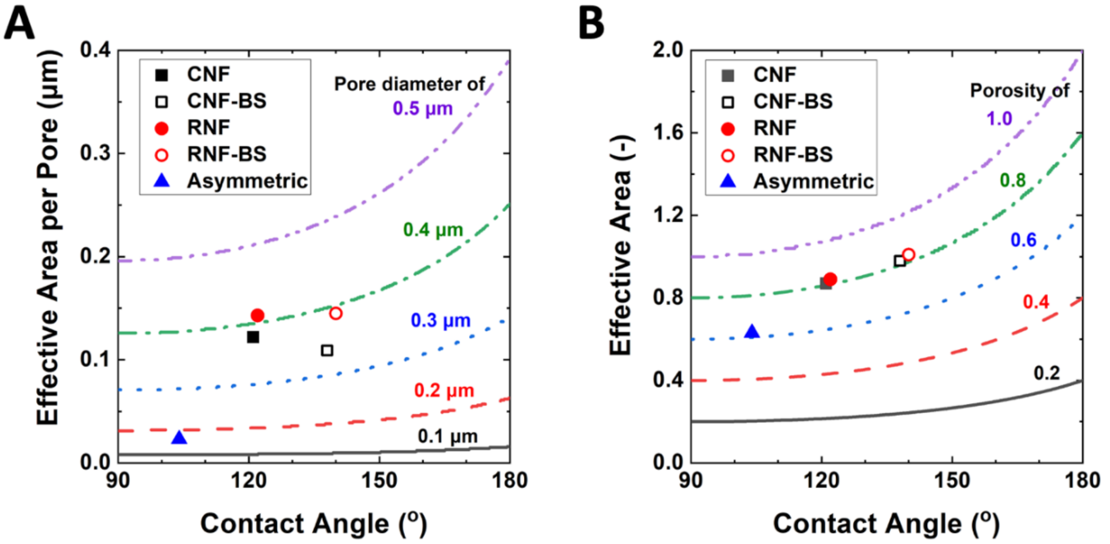

Fig. 7. Effective area of evaporation per pore (Eq. 11) and effective area (Eq. 13) of membranes as a function of contact angle.

3.2. Membrane distillation performance

Water flow in MD is generated by the vapor pressure difference across the membrane and therefore, the temperature difference can be the most critical factor as shown in **Fig. 8**. With the permeate at 20 °C, the water flux gradually increased as a function of the feed temperature between 50 to 80 °C, whereas the NaCl rejection was constant at around 99.98 % for the neat nanofibres and around 99.99% with the bead-on-strings morphology. Due to the great porosity of the nanofibre membranes, they experienced a more significant increase in the water flux as compared to the asymmetric membrane. Despite the similar porosity, the nanofibres with the bead-on-string morphology demonstrated a greater water flux than the neat nanofibres for both random and crosshatched samples, based on their larger effective area of evaporation. In terms of the nanofibre orientations (random or crosshatched), the crosshatched membranes (CNF and CNF-BS) exhibited higher water flux than the randomly oriented membranes (RNF and RNF-BS). Most characteristics of these membranes are similar such as porosity, pore size or contact angle, with the only difference the tortuosity and structural parameter. The more uniform pore structures of the crosshatched membranes and their lower tortuosity can reduce the membrane resistance, leading to the higher water flux. Despite the highest water flux being achieved when the feed is at 80 °C, the feed temperature was fixed to 70 °C for further experiments as this temperature is more achievable using renewable energy sources.

Crossflow velocity or flowrate, which is related to Reynolds number, often becomes an important parameter in membrane separation, because it effects the thickness of the liquid boundary layer [18]. As the flowrate increases, the boundary layer thickness decreases and both temperature and concentration polarisation are minimised. Temperature polarisation affects the membrane performance as any temperature gradient in the boundary layer reduces the driving force for evaporation [35]. Further, excessive concentration polarisation can lead to the crystallisation of salt at the membrane pores, leading to possible pore blockage in long-term operation. For all the membranes studied here, water flux increased when the feed flowrate increased to around 100 to 150 mL min^{-1} (Fig. 8c), corresponding to a Reynolds number of 1500. The MD water flux then became nearly constant, indicating that the resistance from the boundary layer is less significant. The same trend was observed regardless of the types of membranes in this study. The permeate solution conductivity as an indication of NaCl rejection was unchanged with Reynolds number, which means the pores of membranes stayed dry even at high flowrate and only water vapour permeated through the pores.

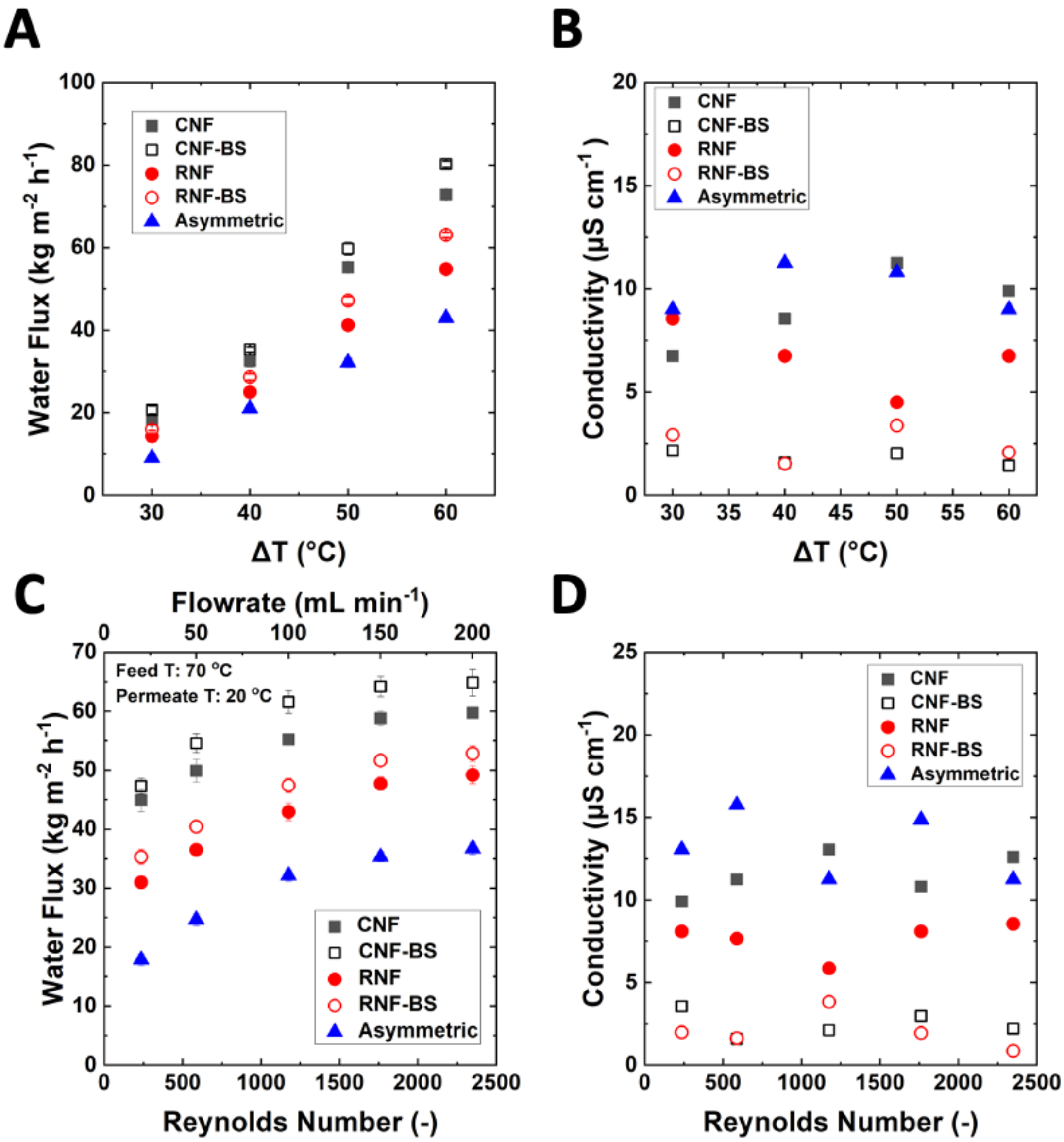

Fig. 8. Water desalination properties in DCMD as a function of (a, b) the temperature difference when the permeate at 20 °C, and (c, d) the Reynolds number of feed flow.

The membrane performance during long-term operation was investigated for 100 h continuous operation as described in **Fig. 9**. Many membranes reported in literature have experienced pore wetting over such timeframes, decreasing the water flux and salt rejection. The first indication of membrane wetting is a flux decline, as the liquid water blocking the membrane pores enters the internal structure under the influence of capillary forces. This is further evidenced by a dramatic increase in the conductivity in the permeate, indicating the presence of salt [7]. The nanofibre membranes also experienced the initial flux decline around 5 to 15 %, indicating the partial pore blockage by liquid water. However, this liquid water only stayed on the pore surface as the NaCl rejection stayed constant for 100 h. The improved hydrophobicity of CNF-BS and RNF-BS membranes even restricted the partial wetting evidenced by the water flux decline in 5-7 %. However, the asymmetric membranes were experienced almost 30 % decline of water flux with slight increase in conductivity. The structural stability of the nanofibre membranes was confirmed by SEM images after the long-term operation as shown in **Fig. 10.** Both the nanofibrous and bead-on-string morphology remained unchanged.

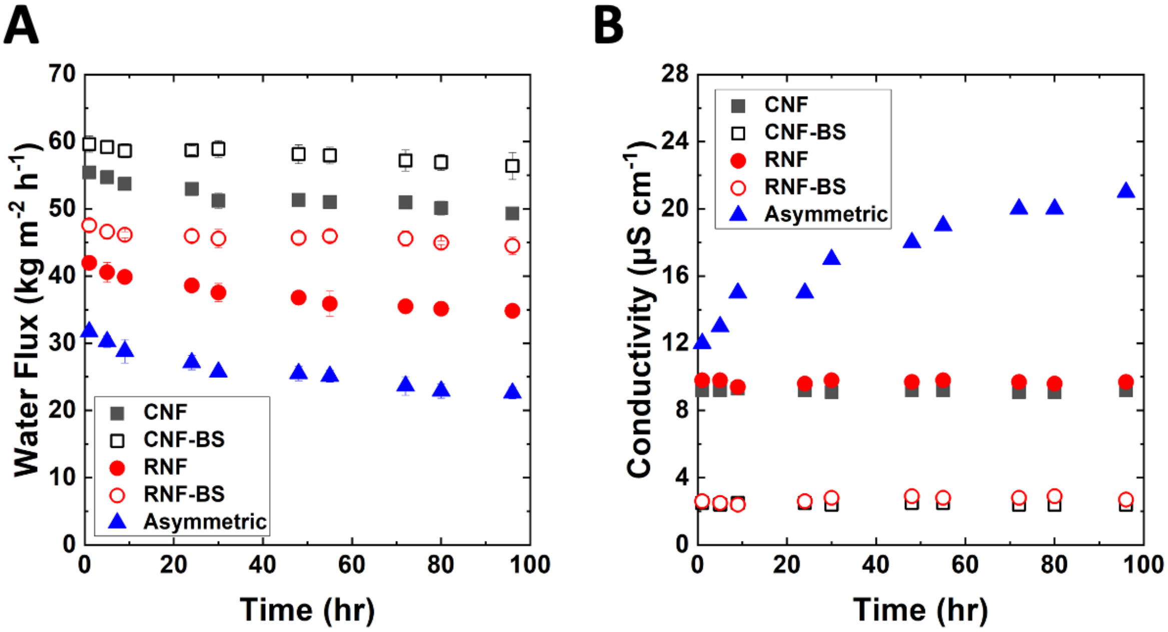

Fig. 9. Water flux (a) and NaCl rejection (b) performance over an extended operation time.

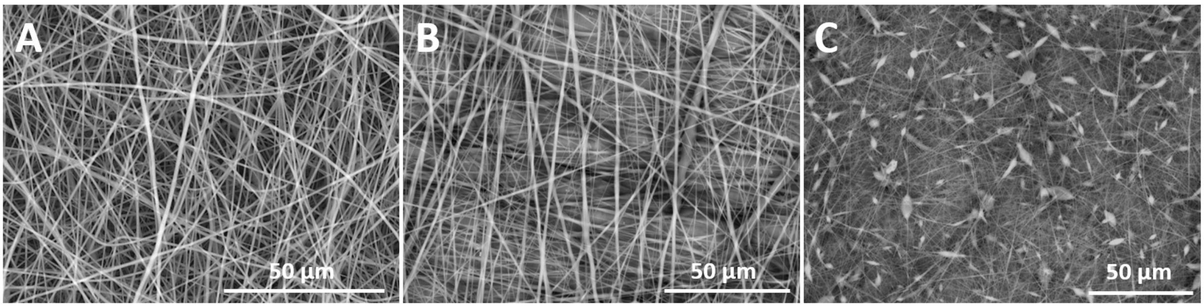

Fig. 10. SEM images of electrospun membranes of (a) random, (b) crosshatched, and (c) bead-on-string nanofibres after 100 h of continuous operation.

The performance of the membranes is summarised in **Table 2** along with other PVDF-based membranes developed for DCMD. The water flux and NaCl rejection are collected from results available with 35 g L^{-1} (or 3.5 wt%) solution and a temperature difference at 40 °C. PVDF-HFP nanofibre membranes prepared from commercial PVDF-HFP polymer exhibited similar performance to the RNF membranes despite having different pore size, porosity and hydrophobicity. Other PVDF-based membranes are mostly nanocomposite or surface-modified to enhance their hydrophobicity, therefore, demonstrating great contact angle over 140 °. However, such modifications can be complicated and expensive for membrane fabrication. The CNF-BS membranes with the modified nanofibre morphology in this study, however, show similar or even greater water flux than other membranes reported, without the need for chemical modifications.

Table 2. Membrane characteristics and desalination performance of PVDF-based nanofibre membranes.

	Pore size (µm)	Porosity (%)	Contact angle (°)	Water flux (kg m^{-2} h^{-1})	NaCl rejection (%)	Reference
PVDF-HFP CNF	0.38	81	121	33	99.98	This study
PVDF-HFP CNF-BS	0.34	82	138	35	99.99	
PVDF-HFP RNF	0.41	82	122	25	99.98	
PVDF-HFP	0.58	89	149	22	99.98	[22]
PVDF-HFP-CNT	0.29	84	159	30	99.99	

PVDF-CNT-FAS	0.18	75	180	32	n/a	[36]
TiO_2-FTCS-PVDF	0.81	57	157	73	99.99	[37]
PVDF-HFP-CNT	1.12	89	150	48	99.9	[38]
PDMS/silica/PVDF	0.81	88	170	28	99.99	[39]

The long-term performance stability can also be affected by crystallisation of inorganic salt crystals, which involves heterogeneous nucleation [9, 28, 40]. Although the crystallisation of well-ordered crystals by homogeneous nucleation is preferable to reduce fouling (Path 1), the activation energy of nucleation is reduced due to the interaction of the salt molecules with the membrane surface, resulting in nucleation earlier within the metastable phase (Path 2) to form large, but less-ordered crystals (**Fig. 11a**). Moreover, the presence of pores on membrane provides a channel for rapid mass transfer, favourable for heterogeneous nucleation where a high level of supersaturation can occur due to the physical entrapment of salt molecules within these pores. Although ΔG_{hom} is always larger than ΔG_{het}, heterogeneous nucleation can be minimised when the ratio ($\Delta G_{het}/\Delta G_{hom}$), calculated from Equation 10, is close to 1.0 (**Fig. 11b**). Hydrophobic membranes facilitate homogeneous nucleation by minimising the contact area of solutes with the membrane. The innate hydrophobicity of PVDF-HFP is not sufficient to prevent heterogeneous nucleation as compared with other typical hydrophobic polymers such as PTFE, but the modification to nanofibrous membranes increases the hydrophobicity, leading to more homogeneous nucleation. In particular, the CNF-BS and RNF-BS membranes with $\Delta G_{het}/\Delta G_{hom}$ values of around 0.9 have the lowest possibility of crystallisation on the pore surface, which will lead to stable long-term operation.

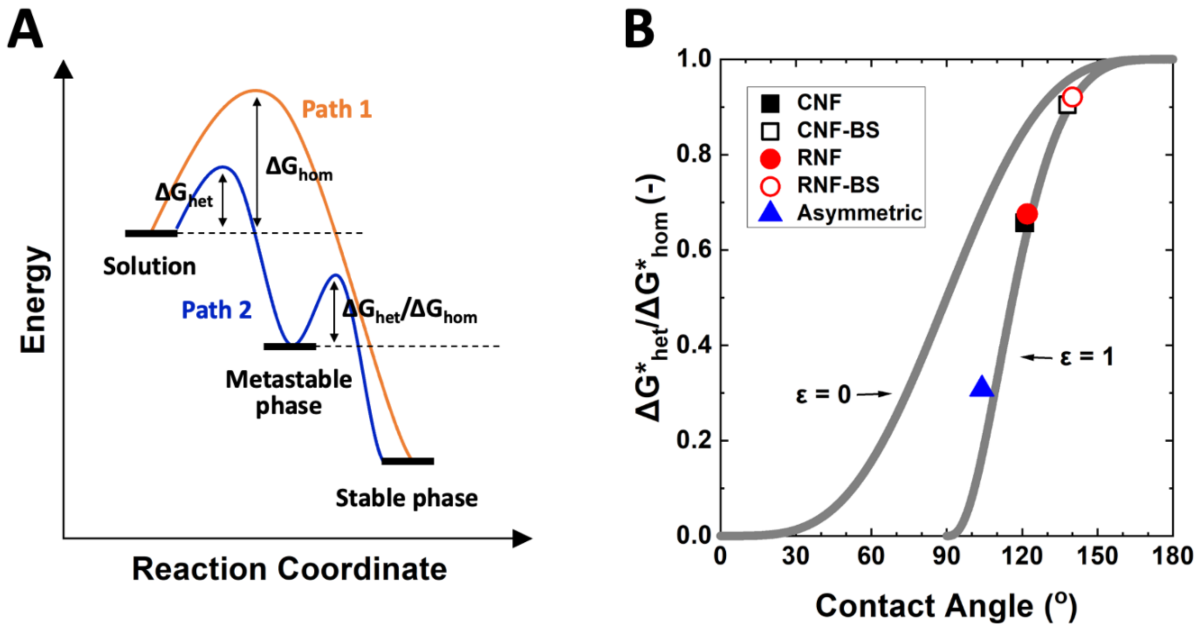

Fig. 11. (a) Different pathway of crystallisation in homogeneous and heterogeneous nucleation. (b) $\Delta G_{het}/\Delta G_{hom}$ based on the contact angle and membrane porosity (Equation 10).

4. Conclusions

In summary, nanofibrous structures of PVDF-HFP membranes were fabricated in a crosshatched morphology with additional surface layers of bead-on-strings, demonstrating improved water flux in DCMD. The alignment and lamination of the nanofibres by electrospinning using a rotating drum collector successfully produced these crosshatched membranes, reducing the tortuosity and leading to decreased mass transfer resistance and enhanced water vapour transport. The additional layer of the bead-on-strings on the nanofibre membranes further increased the hydrophobicity and the effective area of evaporation, resulting in improved water flux and a reduced tendency towards heterogeneous salt crystallisation. The novel crosshatched membranes also demonstrated stable operations for 100 h without decreasing water flux and NaCl rejection.

Acknowledgement

This work was supported by Australian Research Council under the Discovery Projects Scheme (DP190102253) and Discovery early Career Researcher Award Scheme (DE220100135). We also acknowledge the Materials Characterisation and Fabrication Platform (MCFP) at the University of Melbourne and the Victorian Node of the Australian National Fabrication Facility (ANFF) for their technical assistance with the use of electron microscopes.

References

[1] M.-A.A. Hejazi, O.A. Bamaga, M.H. Al-Beirutty, L. Gzara, H. Abulkhair, Effect of intermittent operation on performance of a solar-powered membrane distillation system, Sep. Purif. Technol., 220 (2019) 300-308.

[2] F.E. Ahmed, B.S. Lalia, R. Hashaikeh, N. Hilal, Alternative heating techniques in membrane distillation: A review, Desalination, 496 (2020) 114713.

[3] A. Ruiz-Aguirre, J.A. Andrés-Mañas, J.M. Fernández-Sevilla, G. Zaragoza, Experimental characterization and optimization of multi-channel spiral wound air gap membrane distillation modules for seawater desalination, Sep. Purif. Technol., 205 (2018) 212-222.

[4] R. Ullah, M. Khraisheh, R.J. Esteves, J.T. McLeskey, M. AlGhouti, M. Gad-el-Hak, H. Vahedi Tafreshi, Energy efficiency of direct contact membrane distillation, Desalination, 433 (2018) 56-67.

[5] N.A.S. Elminshawy, M.A. Gadalla, M. Bassyouni, K. El-Nahhas, A. Elminshawy, Y. Elhenawy, A novel concentrated photovoltaic-driven membrane distillation hybrid system for the simultaneous production of electricity and potable water, Renewable Energy, 162 (2020) 802-817.

[6] Y.M. Lee, E. Drioli, Membrane Distillation: Materials and Processes, Nova Science Publishers, Incorporated, 2020.

[7] H. Chamani, J. Woloszyn, T. Matsuura, D. Rana, C.Q. Lan, Pore wetting in membrane distillation: A comprehensive review, Progress in Materials Science, 122 (2021) 100843.

[8] M. Rezaei, D.M. Warsinger, J.H. Lienhard V, M.C. Duke, T. Matsuura, W.M. Samhaber, Wetting phenomena in membrane distillation: Mechanisms, reversal, and prevention, Water Res., 139 (2018) 329-352.

[9] S.H. Park, J.H. Kim, S.J. Moon, E. Drioli, Y.M. Lee, Enhanced, hydrophobic, fluorine-containing, thermally rearranged (TR) nanofiber membranes for desalination via membrane distillation, J. Membr. Sci., 550 (2018) 545-553.

[10] N. Thomas, M.O. Mavukkandy, S. Loutatidou, H.A. Arafat, Membrane distillation research & implementation: Lessons from the past five decades, Sep. Purif. Technol., 189 (2017) 108-127.

[11] L. Eykens, K. De Sitter, C. Dotremont, L. Pinoy, B. Van der Bruggen, Membrane synthesis for membrane distillation: A review, Sep. Purif. Technol., 182 (2017) 36-51.

[12] X. An, Z. Liu, Y. Hu, Amphiphobic surface modification of electrospun nanofibrous membranes for anti-wetting performance in membrane distillation, Desalination, 432 (2018) 23-31.

[13] R. Ding, S. Chen, H. Xuan, B. Li, Y. Rui, Green-solvent-processed amphiphobic polyurethane nanofiber membranes with mechanically stable hierarchical structures for seawater desalination by membrane distillation, Desalination, 516 (2021) 115223.

[14] C. Ji, Z. Zhu, L. Zhong, W. Zhang, W. Wang, Design of firm-pore superhydrophobic fibrous membrane for advancing the durability of membrane distillation, Desalination, 519 (2021) 115185.

[15] Q. Su, J. Zhang, L.-Z. Zhang, Fouling resistance improvement with a new superhydrophobic electrospun PVDF membrane for seawater desalination, Desalination, 476 (2020) 114246.

[16] S. Kim, D.E. Heath, S.E. Kentish, Robust and Superhydrophobic PTFE Membranes with Crosshatched Nanofibers for Membrane Distillation and Carbon Dioxide Stripping, Advanced Materials Interfaces, 9 (2022) 2200786.

[17] S. Kim, D.E. Heath, S.E. Kentish, Composite Membranes with Nanofibrous Cross-Hatched Supports for Reverse Osmosis Desalination, ACS Appl. Mater. Interfaces, 12 (2020) 44720-44730.

[18] S. Kim, D.E. Heath, W.H. Lee, Y.M. Lee, S.E. Kentish, Thermally rearranged nanofibrous composite membranes for carbon dioxide absorption and stripping, J. Membr. Sci., 654 (2022) 120518.

[19] S. Kim, D.E. Heath, S.E. Kentish, Improved carbon dioxide stripping by membrane contactors using hydrophobic electrospun poly (vinylidene fluoride-co-hexafluoro propylene)(PVDF-HFP) membranes, Chem. Eng. J., 428 (2022) 131247.

[20] S. Li, L. Li, J. Zhong, R. Ma, X. Xu, H. Wu, Y. Yu, Engineering beads-on-string structural electrospun nanofiber Janus membrane with multi-level roughness for membrane distillation, Desalination, 539 (2022) 115950.

[21] L. Zhou, C.L. Li, P.T. Chang, S.H. Tan, A.L. Ahmad, S.C. Low, Intrinsic microspheres structure of electrospun nanofibrous membrane with rational superhydrophobicity for desalination via membrane distillation, Desalination, 527 (2022) 115594.

[22] L.D. Tijing, Y.C. Woo, W.-G. Shim, T. He, J.-S. Choi, S.-H. Kim, H.K. Shon, Superhydrophobic nanofiber membrane containing carbon nanotubes for high-performance direct contact membrane distillation, J. Membr. Sci., 502 (2016) 158-170.

[23] J.A. Franco, S.E. Kentish, J.M. Perera, G.W. Stevens, Poly(tetrafluoroethylene) Sputtered Polypropylene Membranes for Carbon Dioxide Separation in Membrane Gas Absorption, Ind. Eng. Chem. Res., 50 (2011) 4011-4020.

[24] M. Rahbari-sisakht, A.F. Ismail, T. Matsuura, Effect of bore fluid composition on structure and performance of asymmetric polysulfone hollow fiber membrane contactor for CO2 absorption, Sep. Purif. Technol., 88 (2012) 99-106.

[25] J. Geens, B. Van der Bruggen, C. Vandecasteele, Transport model for solvent permeation through nanofiltration membranes, Sep. Purif. Technol., 48 (2006) 255-263.

[26] N.Y. Yip, A. Tiraferri, W.A. Phillip, J.D. Schiffman, M. Elimelech, High Performance Thin-Film Composite Forward Osmosis Membrane, Environ. Sci. Tech., 44 (2010) 3812-3818.

[27] M. Volmer, Nucleus formation in supersaturated systems, Z. phys. Chem., 119 (1926) 277-301.

[28] G. Di Profio, E. Curcio, E. Drioli, Supersaturation control and heterogeneous nucleation in membrane crystallizers: facts and perspectives, Ind. Eng. Chem. Res., 49 (2010) 11878-11889.

[29] E. Curcio, E. Fontananova, G. Di Profio, E. Drioli, Influence of the structural properties of poly (vinylidene fluoride) membranes on the heterogeneous nucleation rate of protein crystals, J. Phys. Chem. B, 110 (2006) 12438-12445.

[30] K. Tonsomboon, A.L. Butcher, M.L. Oyen, Strong and tough nanofibrous hydrogel composites based on biomimetic principles, Mater. Sci. Eng. C, 72 (2017) 220-227.

[31] T.-D. Lu, B.-Z. Chen, J. Wang, T.-Z. Jia, X.-L. Cao, Y. Wang, W. Xing, C.H. Lau, S.-P. Sun, Electrospun nanofiber substrates that enhance polar solvent separation from organic compounds in thin-film composites, J. Mater. Chem. A, 6 (2018) 15047-15056.

[32] X. Song, Z. Liu, D.D. Sun, Nano gives the answer: breaking the bottleneck of internal concentration polarization with a nanofiber composite forward osmosis membrane for a high water production rate, Adv. Mater., 23 (2011) 3256-3260.

[33] J.M.C. Puguan, H.-S. Kim, K.-J. Lee, H. Kim, Low internal concentration polarization in forward osmosis membranes with hydrophilic crosslinked PVA nanofibers as porous support layer, Desalination, 336 (2014) 24-31.

[34] W. Jang, Y. Park, C. Park, Y. Seo, J.-H. Kim, J. Hou, H. Byun, Regulating the integrity of diverse composite nanofiber membranes using an organoclay, J. Membr. Sci., 598 (2020) 117670.

[35] A.A. Alanezi, M.R. Safaei, M. Goodarzi, Y. Elhenawy, The effect of inclination angle and reynolds number on the performance of a direct contact membrane distillation (DCMD) process, Energies, 13 (2020) 2824.

[36] Y. Wang, M. Han, L. Liu, J. Yao, L. Han, Beneficial CNT intermediate layer for membrane fluorination toward robust superhydrophobicity and wetting resistance in membrane distillation, ACS Appl. Mater. Interfaces, 12 (2020) 20942-20954.

[37] L.-F. Ren, F. Xia, V. Chen, J. Shao, R. Chen, Y. He, TiO2-FTCS modified superhydrophobic PVDF electrospun nanofibrous membrane for desalination by direct contact membrane distillation, Desalination, 423 (2017) 1-11.

[38] A. Kyoungjin An, E.-J. Lee, J. Guo, S. Jeong, J.-G. Lee, N. Ghaffour, Enhanced vapor transport in membrane distillation via functionalized carbon nanotubes anchored into electrospun nanofibres, Sci. Rep., 7 (2017) 41562

[39] Y. Liao, G. Zheng, J.J. Huang, M. Tian, R. Wang, Development of robust and superhydrophobic membranes to mitigate membrane scaling and fouling in membrane distillation, J. Membr. Sci., 601 (2020) 117962.

[40] J.H. Kim, S.H. Park, M.J. Lee, S.M. Lee, W.H. Lee, K.H. Lee, N.R. Kang, H.J. Jo, J.F. Kim, E. Drioli, Y.M. Lee, Thermally rearranged polymer membranes for desalination, Energy Environ. Sci., 9 (2016) 878-884.